ACS APPLIED OPTICAL MATERIALS

pubs.acs.org/acsaom Article

Simultaneous Optical Trapping and Electromagnetic Micromanipulation of Ferromagnetically Doped $NaYF_4$ Microparticles

Gokul Nalupurackal, Gunaseelan Murugan, Muruga Lokesh, Rahul Vaippully, Amit Chauhan, Birabar Ranjit Kumar Nanda, Chandran Sudakar, Hema Chandra Kotamarthi, Priyankan Datta, Pallab Sinha Mahapatra, Anita Jannasch, Erik Schäffer, Senthilselvan Jayaraman, and Basudev Roy*

Cite This: *ACS Appl. Opt. Mater.* 2023, 1, 615−622 Read Online

ACCESS | Metrics & More | Article Recommendations | Supporting Information

ABSTRACT: Optical trapping allows the trapping and manipulation of dielectric microparticles. However, full control over all six degrees of freedom of the trapped object is challenging. Here, we use ferromagnetic iron-doped upconversion microparticles for simultaneous optical trapping and magnetic micromanipulation that allows full control over all translational and rotational degrees of freedom. These microparticles have a low absorption that allows optical trapping and a high coercivity and saturation magnetization that allow magnetic manipulation. The particles will enable micromanipulation experiments, for example, in single-molecule biophysics.

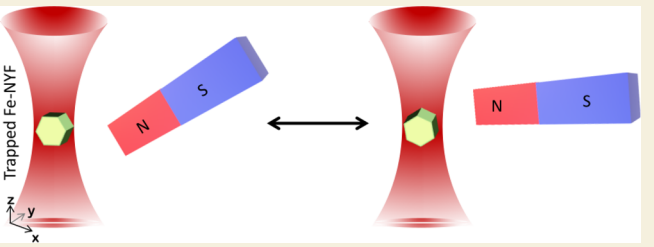

KEYWORDS: *optical tweezers, magnetic tweezers, upconversion particles, ferromagnetic particles, density functional theory*

INTRODUCTION

To understand physical and biological processes at the molecular scale requires the measurement and/or application of displacements, angular motion, force, and torque. Ideally, controlled micromanipulation of all degrees of translational and rotational freedom is desired. The translation is generally performed using optical tweezers[1−3] with some controlled in-plane rotation (can be called yaw[4−7] in airline nomenclature) also being performed. Magnetic tweezers[8,9] are generally used to rotate particles in all senses while applying controlled torques, with some applications of controlled forces. Such micromanipulation also relies heavily on high-spatial and -temporal resolution detection.

Magnetic tweezers are used to manipulate particles with forces ranging over 7 orders of magnitude from 10^{-3} to 10^4 pN. They are highly advantageous for monitoring biological processes under low-force regimes (<0.5 pN) where the biomolecules are minimally perturbed. However, a magnetic field cannot create a stable stationary equilibrium configuration to confine a particle (Earnshaw theorem). Rather, it is employed in the transport of magnetic microparticles such as diamagnetic graphene particles.[10] To achieve spatial confinement of particles in these configurations, special geometries must be employed using a combination of magnetic and other forces[11,12] or sophisticated electromagnets with feedback control.[13] In these experiments, the molecule of interest is typically tethered between a surface and a superparamagnetic particle, and the force is applied via an external magnetic field. In this way, forces and controlled torques in all senses can be applied.[14,15] However, the inability to decouple force and torque application is a major impediment for magnetic tweezers.

Typical magnetic tweezers track the position of particles at an acquisition frequency of ≈50−100 Hz and resolve the subsequent position of a particle along the *z*-axis to ∼1 nm using video cameras.[16−18] Recent improvements to magnetic tweezers based on high-speed complementary metal oxide semiconductor (CMOS) cameras have enhanced the resolution to the subangstrom level at a 1 s bandwidth on individual particles.[19,20] However, it can still be improved with higher-bandwidth measurements, in terms of both speed and accuracy, by using interferometric detection.

Three-dimensional controllable manipulation of particles can be easily achieved with optical tweezers,[21,22] and hence, integrating these techniques provides the advantage of both low forces of magnetic tweezers and high spatiotemporal detection of optical tweezers for monitoring enzymatic processes.[23−25] Few of the early attempts to combine magneto-optical tweezers used a monodisperse polystyrene

Received: November 16, 2022
Accepted: February 3, 2023
Published: February 13, 2023

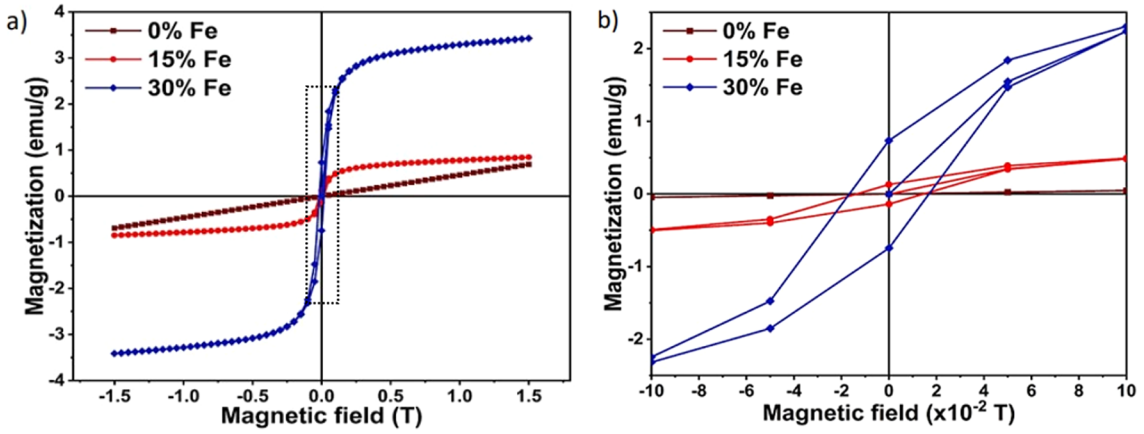

Figure 1. (a) Room-temperature VSM hysteresis curve of Fe-15 and Fe-30 NYF, compared with that of the pristine NYF sample. (b) Enlarged view of the curve from which the magnetic remanence and coercivity are calculated.

substrate coated in a layer of chromium oxide (CrO_2), which was held together by an outer polystyrene layer[26] and Micromer magnetic beads (3 μm diameter, Micromod, Rostock, Germany) selected for their low magnetic content, permitting good optical trapping.[27] The chromium oxide shell material, although suggested to be ferromagnetic, loses this behavior at room temperature, and exhibits low magnetization values. In all of these particles, the presence of magnetic materials makes optical trapping complicated due to the high optical absorption.

Here, we present an alternative strategy in which the tracer particle is not only highly magnetic but also easily optically trappable. This provides the best of magnetic forces in conjugation with high spatiotemporal detection that the optical tweezers provide via interferometric detection with the quadrant photodiodes. We show that Fe-doped upconversion $NaYF_4$:Yb,Er particles (Fe-NYF) have ferromagnetic features, yet the refractive index is quite conducive to optical tweezers measurements (the lattice $NaYF_4$ has a refractive index of 1.47), even for particles as large as 5 μm, with a large saturation magnetization of 1 A m^2 kg^{-1}. The upconversion $NaYF_4$:Yb,Er (NYF) nonmagnetic particles have been routinely used with optical tweezers.[28−30] Also, the emission properties of these particles at different wavelengths can be enhanced through Fe doping,[31,32] and external magnetic fields are employed to modulate the spectral lines of such a particle through Zeeman splitting and shifting.[33] However, for the first time, the magnetic properties of these NYFs through co-doping with Fe are being explored. We show that this co-doped particle can be held in optical tweezers while the magnetic field could be used to turn the particle in all three degrees of freedom, namely, yaw, pitch,[29,34−37] and roll,[38] in airline nomenclature. Controlled in-plane rotations of single ferromagnetic magnetite nanowires using external magnetic fields were reported,[39] but the detection of the rotations lacks the high spatiotemporal resolution that our system offers.

RESULTS

Magnetic Properties of Fe-15, Fe-30 NYF

The magnetic properties of pristine $NaYF_4$:Yb,Er upconversion particles (Fe-NYF) and Fe-doped $NaYF_4$:Yb,Er upconversion particles with different degrees of doping (15 and 30 atom %, Fe-15 NYF and Fe-30 NYF, respectively) are measured using a vibrating sample magnetometer (Figure 1). The pristine sample exhibits linear $M-H$ curves showing paramagnetic behavior. However, the Fe-NYFs are ferromagnetic as seen from the S-shaped curve. The magnetization of the Fe-15 NYF sample is ≈1 A m^2 kg^{-1} at 1.5 T; however, this increases to ≈3.5 A m^2 kg^{-1} (at 1.5 T) for Fe-30 NYF upconversion particles. This material can be placed in the context of standard superparamagnetic particles routinely used in the community of magnetic tweezers, like Dynabeads M-280,[40] which have a saturation magnetization of 6 A m^2 kg^{-1}. It should be noted that the magnetization, in our particles, predominantly arises from the Fe dopant effect in NYF upconversion particles. Previously, ferromagnetic features of $NaLuF_4$:Er^{3+}, Yb^{3+}-based upconversion particles were reported,[41] and their transition from ferromagnetic state to paramagnetic state was observed with an increase in the doping concentration of the Gd^{3+} ion. The Gd^{3+} ion is paramagnetic, and hence, an increase in the concentration of this ion makes the particle more paramagnetic. Such changes in saturation magnetization are associated with the changes in crystalline structure caused by the excess doping.[42]

In the powder of the particles, a low concentration (<1%) of Fe_2O_3 phase regions that are predominantly unstructured and can easily be distinguished from the hexagonally shaped NYF is present. If the magnetization contribution arose from Fe_2O_3, the magnetization values would have been much lower than 0.01 A m^2 kg^{-1}.[43,44] The realization of ferromagnetic properties in Fe-NYF upconversion particles itself is interesting and has not been reported hitherto. The hysteresis curves of these magnetic particles also show discernible coercivity, i.e., ≈20 mT. The magnetic properties of the particles with magnetization around a few amperes square meter per kilogram and a coercivity of ≈20 mT ideally suit the requirement whereby magnetic forces can be controlled by an externally applied magnetic field.

Why Ferromagnetic: Electronic Structure Calculations

To gain more insights into the experimental observations of ferromagnetism in Fe-NYF, we examined the electronic structure by performing density functional theory (DFT) calculations within the framework of generalized gradient approximation (GGA) as implemented in the Vienna ab initio simulation package (VASP). For this purpose, we employed a supercell geometry and designed the composition $NaY_{2/3}Yb_{1/6}Fe_{1/6}F_4$. Er doping is not taken into account as it has a very low concentration in the experimentally synthesized

https://doi.org/10.1021/acsaom.2c00161
ACS Appl. Opt. Mater. 2023, 1, 615−622

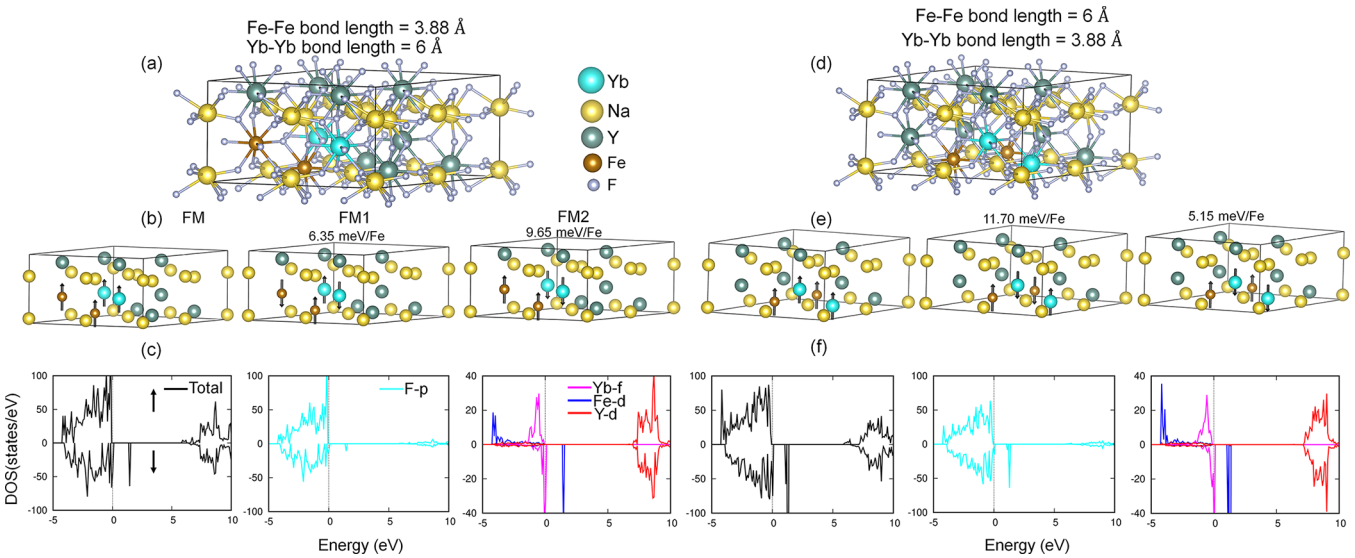

Figure 2. Crystal structures of $NaY_{2/3}Yb_{1/6}Fe_{1/6}F_4$ with Fe−Fe and Yb−Yb bond lengths of 3.88 and 6 Å and vice versa (top). Designed magnetic configurations (middle): FM, FM1, and FM2. The energetics are shown with respect to the stable FM state. Spin- and atom-resolved total density of states of the most stable FM configuration (bottom).

particles. The supercell structures for the aforementioned composition with two Fe and two Yb atoms are shown in Figure 2. The structural and computational details are provided in Materials and Methods. We have considered two doping arrangements. In one of them, the Fe−Fe (Yb−Yb) bond length is 3.88 (6) Å, while in the other, it is 6 (3.88) Å (see Figure 2a,d). For both arrangements, we have designed three magnetic configurations, namely, ferromagnet (FM), ferrimagnet1 (FM1), and ferrimagnet2 (FM2) (see the middle panel of Figure 2). The density of states for the energetically most stable FM configuration is shown in the bottom panel of Figure 2.

The FM state is most stable compared to the ferrimagnetic states for both doping arrangements and exhibits large (≈4 μ_B) and weak (≈0.7 μ_B) spin magnetic moments in Fe and Yb. The formation of a large (weak) spin moment in Fe and Yb can be understood from the total density of states of Fe (Yb). Being the impurity states, the Fe-d and Yb-f states are well localized. For Fe, the majority spin-up channel is completely occupied whereas the minority spin-down channel is unoccupied, giving rise to a large spin magnetic moment in Fe inferring a 3+ charge state that is also further confirmed by the XPS measurements. A detailed electronic structure analysis suggests that there is a reasonable hybridization among the Fe-d and F-p states leading to an induced magnetization in the latter. As a result, the total magnetization per Fe is ≈5.1 μ_B with 4 μ_B contributed by the Fe-d states, and the rest is contributed by the dispersive F-p states. As Yb also possesses a 3+ charge state and hence a $4f^{13}$ electronic configuration, the down-spin channel is dominantly occupied and leads to the formation of a very weak local moment compared to that of Fe. In the absence of Fe doping, Yb demonstrates paramagnetism. However, with Fe doping, the Yb spins develop ferromagnetic ordering with Fe to amplify the net magnetization. With an increased Fe−Fe bond length, the FM state remains energetically most favorable. Hence, the system exhibits a robust FM state, which is in accordance with the experimental observations in this work.

Application: Magneto-optical Trapping of Fe-NYF

One such Fe-15 NYF upconversion particle was optically trapped, and then a magnet moved (or current in an electromagnet changed) in the proximity as indicated in Figure S1. We also mention here that the refractive indices for Fe-15 NYF and NYF at a 975 nm pump resonance are $n_{Fe-15\ NYF}$ = 1.479 + i0.0029 and n_{NYF} = 1.463 + i0.0014, while $n_{Fe-15\ NYF}$ = 1.477 + i0.0011 and n_{NYF} = 1.461 + i0.0008 at 1050 nm. Thus, the Fe-15 NYF material has a higher absorption at 975 nm than NYF does, while the absorption remains low for optical trapping at 1050 nm. In comparison, haematite and magnetite have values of $n_{hematite}$ = 2.504 + i0.038 and $n_{magnetite}$ = 2.112 + i0.365, respectively, at a laser wavelength of 1064 nm, which makes them difficult to trap for diameters of >400 nm, not to mention much higher absorption leading to significant heating upon illumination.

The power spectral density for an optically trapped Fe-15 NYF at a wavelength of 1064 nm, modulated with an alternating magnetic field at 10 Hz, is shown in Figure 3a (and fitted to an aliased Lorentzian also accounting for experimental electronic filters[45,46]), and the subsequent motion of the particle in the x direction in the presence of the field is shown in Figure 3b. It may be noted here that the lateral position of the particle has been detected to a bandwidth of 10 kHz using the interferometric detection made possible by the optical tweezers,[47,48] something difficult to do with video tracking at high resolution. The measured force due to the magnetic field is 82 ± 4 fN. It can be mentioned here that, generally, magnetic tweezers have a detection accuracy of ∼50 fN[18,27] due to the usage of video microscopy for tracking. It may also be noted here that if the motion due to the magnetic field can be calibrated using, for instance, video microscopy, a new technique of active calibration of the PSD can also be envisaged. The exact details of such a calibration are however beyond the scope of this work.

We find that the particle turns in all rotational senses. First, we turn in the pitch sense as indicated in Figure 4. The out-of-plane motion is visible. The region indicating the out-of-plane motion was then selected in the image sequence, and a time

https://doi.org/10.1021/acsaom.2c00161
ACS Appl. Opt. Mater. 2023, 1, 615−622

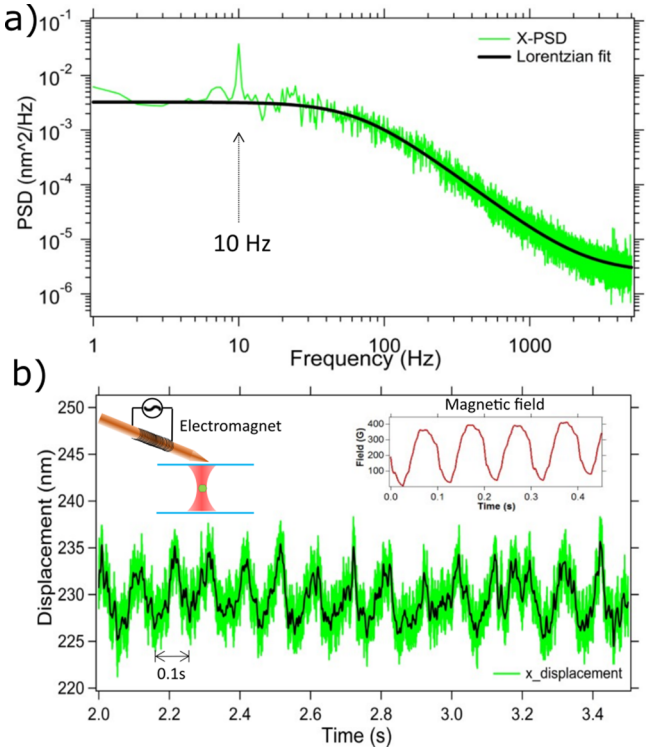

Figure 3. (a) Power spectral density (PSD) of horizontal displacements (x displacements) of an optically trapped Fe-15 NYF in the presence of an alternating magnetic field [300 G (peak to peak) at 10 Hz]. We show that the PSD is being modulated at 10 Hz, the frequency of applied AMF. The optical trap is calibrated with a displacement sensitivity of 1.03 ± 0.3 μm/V. The corner frequency (f_c) is 89 ± 5 Hz; hence, the trap stiffness is found to be 0.0084 ± 0.0005 pN/nm. (b) Corresponding displacement time series of the same trapped particle. The inset shows the applied ac magnetic field with a frequency of 10 Hz. The displacements are recorded using optical interferometry with a sensitivity greater than that available with video tracking for the axial direction motion.

series was recorded to ascertain the dynamics (see Figure 4g). Then we turn the particle in the in-plane yaw sense, as indicated in panels h and i of Figure 4. Then, we direct our attention to turn the particle in the roll sense as indicated in Figure 5. Here, like the pitch motion, the region of the image indicating the roll motion was selected, nd a time series of the total intensity in that region was recorded to determine the dynamics. In this way, the roll motion can also be detected using the camera.

DISCUSSION

Figure S4 shows the structural information of $NaYF_4$:Yb,Er particles at different concentrations of Fe, which is obtained from Rietveld refinement using the FullProf software. The Rietveld refinement is carefully performed by considering the crystallographic phases of $NaYF_4$. The prepared samples crystallize in a hexagonal structure of $NaYF_4$ (β-$NaYF_4$) in space group $P63/m$. The goodness of fit is evidenced by the R-factors of the refinement as given in the table. Despite the substitution of Fe^{3+} at the Y^{3+} site, the structure remains in the hexagonal phase. The estimated lattice parameters are listed in the table. The decrease in the lattice parameters reveals that the Fe^{3+} with a smaller ionic radius is substituted in the Y^{3+} site, which leads to shrinkage of the lattice. This indicates a decrease in the distance between two 2c sites (i.e., Ln−Ln).

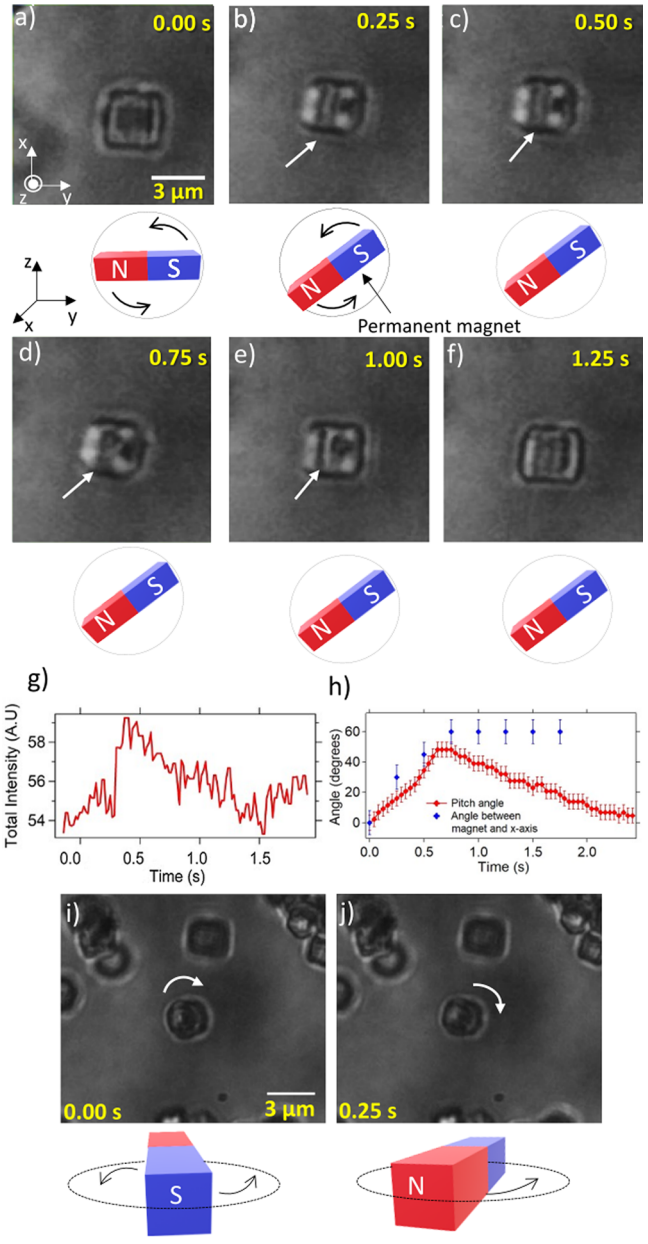

Figure 4. (a−f) Pitch rotational motion of an optically trapped, Fe-15 NYF upconversion particle under the influence of an external magnetic field. (g) Corresponding time series of rotation obtained by video microscopy, where the total intensity inside a rectangular region located at the tip of the arrow in panel b has been considered. (h) Angle by which the centroid of the fringe shown in the rectangle is rotated in the pitch sense and the orientation of the axis of the magnet with respect to the x-axis. (i and j) Yaw rotations of the particle under the influence of the same external magnetic field.

The decrease in the distance between Ln^{3+} and Fe^{3+} facilitates the interaction through 3d−4f coupling in the hexagonal $NaYF_4$ matrix. The Fe-15 NYF samples exhibit a small phase fraction of α-Fe_2O_3 impurity (0.96 wt %) in addition to β-$NaYF_4$. The variation in the electron density in the Fourier maps, which is extracted from the refinement, further confirms the substitution of the Fe^{3+} in the Y^{3+} site. Moreover, if the Fe does not go into the lattice of the β-$NaYF_4$ structure, the diffraction pattern would show a 13 wt % α-Fe_2O_3 impurity phase. The Fe-30 NYF samples also show a β-$NaYF_4$ structure, however, with a higher percentage of the α-Fe_2O_3 (5 wt %)

https://doi.org/10.1021/acsaom.2c00161
ACS Appl. Opt. Mater. 2023, 1, 615−622

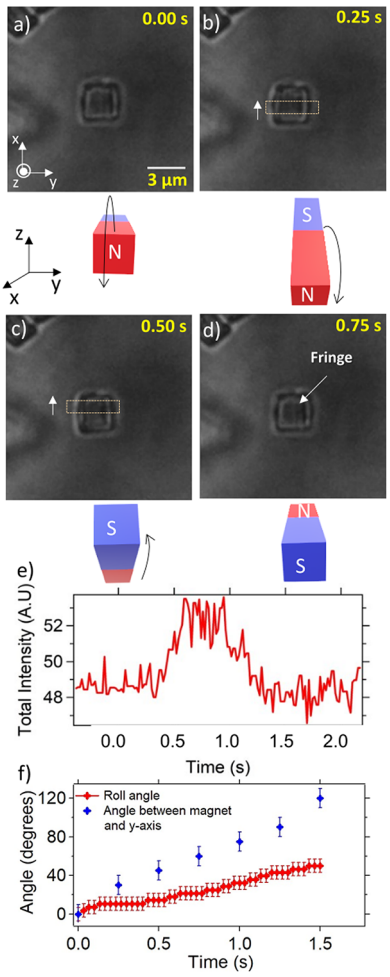

Figure 5. (a–d) Roll rotational motion of an optically trapped Fe-15 NYF upconversion particle under the influence of an external magnetic field. (e) Time series corresponding to the roll motion of the total intensity inside one of the rectangular regions. The marked fringe on the particle is taken as a reference to visualize the out-of-plane roll motion. (f) Roll angle vs time graph, obtained by tracking the centroid of the fringe and the angles at which the external magnet is rotated as a function of time. Arrows near the bar magnet indicate the direction in which it is rotated to generate roll motion.

phase. This implies that a higher concentration of Fe leads to the formation of impurities. In this study, we have used Fe-15 NYF particles as they exhibit optimal magnetization values and a lower impurity concentration is needed for the optical trapping experiments.

These particles show emission at visible wavelengths when illuminated with 975 nm light by multiphoton processes as illustrated in Figure S6c. The spectra for the different configurations of the particle are different (as shown in Figure S6c), which enables the possibility of using the changes in the spectra to determine the pitch rotational motion to a high resolution by illuminating with 975 nm light itself.[49−51] The use of emission from the particle to detect rotational motion has already been demonstrated in ref 49, particularly in the yaw (or in-plane) sense.

These can also then be used to generate continuous rolling motion of a free Fe-NYF upconversion particle using a magnetic field rotating along the out-of-plane sense[52] to make a microrobot. The instantaneous angle at which it is rolling can be determined from the change in its emission spectra.[50] These magnetic particles may also be used as magnetic microrollers on blood artery walls (or any vessel walls), where the surface locomotion properties of such microrollers are determined by the shape anisotropy of the particles[53] and the rotational motion can be detected with high resolution from emission spectra.

CONCLUSIONS

To summarize and conclude, we prepared Fe co-doped $NaYF_4$:Yb,Er upconversion particles that have ferromagnetic properties. We find that a single Fe-doped upconversion particle with a diameter of >3 μm can be optically trapped in three dimensions and the dynamics of such a trapped particle may be controlled in all six dimensions of a rigid body enabling multifarious uses. The optical trap parameters determined from our experiments are close to the results from scattering simulations performed using the T-matrix tool. Via application of an external magnetic field, an optically trapped particle may be rotated in the yaw, pitch, and roll sense. We detect the rotations with a video camera and the translations using a quadrant photodiode. The upconversion properties of the particles are confirmed by their emission spectra. There is also the possibility of using these particles as microrobots by rolling them on surfaces using rotating magnetic fields and detecting the rotation by the change in spectra with a very low power 975 nm light beam. This process can be applied in combining the best of optical tweezers and magnetic forces to enable a new class of experiments in which the application of forces and torques with high-bandwidth accurate position and orientation sensitivity is required. We show the detection sensitivity of magnetic forces of 4 fN, quite difficult to perform with video microscopy. We also envisage the detection of rotational motion, both in plane and out of plane at high resolution, of such hexagonally shaped particles using interferometric microscopy of the laser light. The exact details of such a measurement are, however, beyond the scope of this work.

MATERIALS AND METHODS

$RE(NO_3)_3{\cdot}6H_2O$ (RE = Y, Yb, or Er; 99.99% pure), $Fe(NO_3)_3{\cdot}9H_2O$ (99.999%), and sodium citrate dihydrate (99%) were purchased from Alfa Aesar and used without further purification. Doubly distilled water and C_2H_5OH (Hayman, 99.9%) were used to prepare Fe-NYF upconversion particles.

Preparation

The Fe-doped $NaYF_4$:Yb,Er upconversion particles (Fe-NYF) were prepared by the basic hydrothermal method with some modifications.[29] However, citrate-assisted hydrothermal preparation of Fe-NYF upconversion particles has not yet been reported. To prepare Fe-15 NYF, 0.126 M $Y(NO_3)_3$ (63 atom % Y) and 0.3 M sodium citrate were added to 14 mL of water while the mixture was vigorously magnetically stirred for 10 min. Then, 40 mM $Yb(NO_3)_3$ (20 atom % Yb), 4 mM $Er(NO_3)_3$ (2 atom % Er), and 30 mM $Fe(NO_3)_3$ (15 atom % Fe) in 21 mL of H_2O (taken from Millipore DQ 3, Merck Systems) were added to the sodium citrate solution, which then appeared to be a milky white solution. A transparent solution was obtained by adding 0.5 M NaF in 67 mL of an aqueous solution to the milky white solution and stirred for 1 h. The transparent solution was subsequently transferred to a 200 mL Teflon-lined autoclave that was then tightly sealed. Then, it was heated using a muffle furnace at 200 °C for 12 h. The solution was washed with water and ethanol four times after cooling naturally to room temperature inside the autoclave. The sample in powdery form was collected after drying at 100 °C for 12 h. Similar preparation steps were also followed to prepare Fe-30 NYF except for the changes in the concentrations to 0.06 M

https://doi.org/10.1021/acsaom.2c00161
ACS Appl. Opt. Mater. 2023, 1, 615−622

$Fe(NO_3)_3$ (30 atom % Fe) and 0.096 M $Y(NO_3)_3$ (48 atom % Y). These particles were dispersed in deionized water for the experiment.

Experimental Details

The experiments were performed on a setup made from an optical tweezers kit (OTKB/M, Thorlabs) in the inverted configuration. Either a linearly polarized laser beam (diode laser, LSR1064NL, Lasever) with a wavelength of 1064 nm and a maximum output power of 1.5 W or a linearly polarized 400 mW, 975 nm butterfly laser (CLD1015, Thorlabs) was used to form the optical trap. The laser was tightly focused on the sample chamber using an Olympus 100× objective (1.3 NA, oil immersion type), and a 10× Nikon condenser (0.25 NA, air immersion) was used to collect the forward scattered light from the optical trap as shown in Figure S1. The power at the sample stage of the 1064 nm laser was 65 mW, measured with a power meter (PM100D, Thorlabs) with a head unit (S130C, Thorlabs). A light-emitting diode lamp was used to illuminate the sample from the top via a dichroic mirror, as shown in Figure S1. The forward scattered light was made incident on a quadrant photodiode (QPD) (PDQ80A, Thorlabs) upon reflection from the same dichroic mirror. Interferometric detection, in which the scattered light from the particle and the unscattered light interfered, gave very good position sensitivity,[47,48] enabling high-resolution position determination.

The sample chamber consisted of a 75 mm × 25 mm × 1 mm glass slide (Blue star, number 1 size, English glass) on which the sample was placed using a pipet and mounted with a glass coverslip (Blue star, number 1 size, English glass). The whole system was then inverted and placed on the sample stage. A piezo-electric stage (Thorlabs Nanomax 300) was used to hold the sample between the objective and condenser lenses. A linearly polarized laser beam with a wavelength of 1064 nm was tightly focused on a single UCP, which constituted the optical tweezers. Water was from Millipore (DQ 3, Merck Systems).

The particles tended to aggregate when left unattended. There were some Fe_2O_3 regions in the sample that were clearly distinguishable, having an unstructured morphology compared to the regularly shaped hexagonal particles. When these regions were illuminated with infrared light, we tended to find heating due to absorption and then the aggregate exploded. This is how we obtained individual hexagonal particles.

The magnetic particles were manipulated manually using a ring-type magnet (ceramic ferrite magnet, Perfect Magnet) with an inner radius of 22 mm, an outer radius of 45 mm, and a thickness of 20 mm. A magnetic field of 30 G was produced by this magnet at an axial distance of 8 cm. The magnet was rotated manually with respect to the *x*- and *y*-axes of the piezo stage to produce yaw, pitch, and roll motions of the trapped particle. The response of an optically trapped magnetic upconversion particle to the external field was recorded using a CMOS camera (CS165CU1, Thorlabs). The particles were trapped ∼10 μm from the bottom surface. The entire system was kept at room temperature (25 °C).

Using the same electromagnet, the dynamics of an optically trapped single Fe-30 NYF were controlled. The particle was trapped with a 1064 nm laser at 30 mW, and an alternating magnetic field with a peak-to-peak flux density of 375 G and a frequency of 10 Hz was applied in the vicinity of the optical trap (see the inset of Figure 3). The forward scattered light from the particle was collected using a quadrant photodiode as shown in the schematic diagram (see Figure S1).

Structural and Computational Details

We designed a $NaY_{2/3}Yb_{1/6}Fe_{1/6}F_4$ configuration to theoretically understand the origin of ferromagnetism as observed experimentally. In this configuration, Er doping was not taken into account as it had a very low concentration and had a negligible effect on the electronic and magnetic structure of the system. The $NaY_{2/3}Yb_{1/6}Fe_{1/6}F_4$ configuration was designed by performing the following steps. (i) The $Na_4Y_2F_6$ crystal structure was constructed in space group $P6_3/m$ where the Na, Y, and F atoms occupied the 4*e*, 2*d*, and 6*h* Wyckoff sites, respectively. The 4*e* and 2*d* Wyckoff sites were one-fourth and three-fourth occupied, respectively, whereas the 6*h* site was completely occupied. (ii) The obtained crystal structure was doubled along the *c*-axis. In addition, because the Na 4*e* site was one-fourth occupied, six Na atoms were removed from the structure. One of the Y atoms was replaced by Na as the 2*d* site was shared by Y and Na atoms with three-fourth and one-fourth occupancies, respectively. The resultant crystal structure was $Na_3Y_3F_{12}$. In addition, to design the $NaY_{2/3}Yb_{1/6}Fe_{1/6}F_4$ configuration, a 2 × 2 × 1 supercell was designed from $Na_3Y_3F_{12}$ and four of the Y sites were replaced by two Fe atoms and two Yb atoms (see Figure 2a,d). To determine the plausible origin of ferromagnetism in the system, the first-principles-based density functional theory (DFT) calculations were carried out in the plane-wave basis using the projector-augmented wave potentials[54] as implemented in VASP.[55] The generalized gradient approximation (GGA) was chosen for the exchange-correlation function. The Brillouin zone integration was carried out using a 4 × 4 × 8 and 8 × 8 × 8 Γ-centered k-mesh to achieve the self-consistent ground state and its corresponding density of states. A 400 eV kinetic energy cutoff was chosen for the plane wave basis set.

■ ASSOCIATED CONTENT

Supporting Information

The Supporting Information is available free of charge at https://pubs.acs.org/doi/10.1021/acsaom.2c00161.

Video showing roll motion (AVI)
Video showing pitch motion (AVI)
Video showing yaw motion (AVI)
Video showing animation of particle rotation upon moving the magnet (AVI)
Video showing combined pitch and roll rotation (AVI)
Description of the setup, details of the T-matrix scattering calculation for the trapping feasibility of Fe-NYF, morphology of Fe-NYF, and absorptive and emissive properties of Fe-NYF (PDF)

■ AUTHOR INFORMATION

Corresponding Author

Basudev Roy − *Department of Physics, Quantum Centres in Diamond and Emergent Materials (QuCenDiEM)-group, Micro Nano and Bio-Fluidics (MNBF)-Group, Indian Institute of Technology Madras, Chennai 600036, India;* orcid.org/0000-0003-0737-2889; Email: basudev@iitm.ac.in

Authors

Gokul Nalupurackal − *Department of Physics, Quantum Centres in Diamond and Emergent Materials (QuCenDiEM)-group, Micro Nano and Bio-Fluidics (MNBF)-Group, Indian Institute of Technology Madras, Chennai 600036, India*

Gunaseelan Murugan − *Department of Physics, Quantum Centres in Diamond and Emergent Materials (QuCenDiEM)-group, Micro Nano and Bio-Fluidics (MNBF)-Group, Indian Institute of Technology Madras, Chennai 600036, India; Department of Physics, Rathinam Research Hub, Rathinam College of Arts and Science, Coimbatore 641021, India*

Muruga Lokesh − *Department of Physics, Quantum Centres in Diamond and Emergent Materials (QuCenDiEM)-group, Micro Nano and Bio-Fluidics (MNBF)-Group, Indian Institute of Technology Madras, Chennai 600036, India*

Rahul Vaippully − *Department of Physics, Quantum Centres in Diamond and Emergent Materials (QuCenDiEM)-group,*

https://doi.org/10.1021/acsaom.2c00161
ACS Appl. Opt. Mater. 2023, 1, 615−622

Micro Nano and Bio-Fluidics (MNBF)-Group, Indian Institute of Technology Madras, Chennai 600036, India

Amit Chauhan − *Condensed Matter Theory and Computational Lab, Department of Physics, Indian Institute of Technology Madras, Chennai 600036, India*

Birabar Ranjit Kumar Nanda − *Condensed Matter Theory and Computational Lab, Department of Physics, Indian Institute of Technology Madras, Chennai 600036, India;* orcid.org/0000-0001-8330-4824

Chandran Sudakar − *Center for Atomistic Modelling and Materials Design, Indian Institute of Technology Madras, Chennai 600036, India;* orcid.org/0000-0003-2863-338X

Hema Chandra Kotamarthi − *Department of Chemistry, Indian Institute of Technology Madras, Chennai 600036, India;* orcid.org/0000-0003-0278-1376

Priyankan Datta − *Department of Mechanical Engineering, Indian Institute of Technology Madras, Chennai 600036, India*

Pallab Sinha Mahapatra − *Department of Mechanical Engineering, Indian Institute of Technology Madras, Chennai 600036, India;* orcid.org/0000-0002-4073-9980

Anita Jannasch − *Center for Plant Molecular Biology (ZMBP), University of Tübingen, 72074 Tübingen, Germany*

Erik Schäffer − *Center for Plant Molecular Biology (ZMBP), University of Tübingen, 72074 Tübingen, Germany;* orcid.org/0000-0001-7876-085X

Senthilselvan Jayaraman − *Department of Nuclear Physics, University of Madras, Chennai 600025, India;* orcid.org/0000-0002-6643-0834

Complete contact information is available at: https://pubs.acs.org/10.1021/acsaom.2c00161

Author Contributions

G.N., G.M., M.L., and R.V. performed the experiment and analyzed data. G.M. and S.J. synthesized the particles. A.C., P.D., P.S.M., and B.R.K.N. performed the simulations. C.S. analyzed TEM and XPS data. A.J. and E.S. analyzed data and performed the scattering calculations. B.R. conceptualized the experiment and analyzed data. B.R., C.S., A.C., H.C.K., B.R.K.N., and E.S. wrote the manuscript.

Notes

The authors declare no competing financial interest.

■ ACKNOWLEDGMENTS

The authors thank the Indian Institute of Technology Madras for their seed and initiation grants. This work was also supported by DBT/Wellcome Trust India Alliance Fellowship IA/I/20/1/504900 awarded to B.R. The authors thank HPCE, IIT Madras, for providing the computational facility. This work was also funded by the Department of Science and Technology, India, through Grant CRG/2020/004330. The authors also thank Privita Edwina and Saumendra Bajpai for providing MCF7 cells and putting UCP inside.

■ REFERENCES

(1) Cheng, W.; Arunajadai, S. G.; Moffitt, J. R.; Tinoco, I.; Bustamante, C. Single-base pair unwinding and asynchronous RNA release by the hepatitis C virus NS3 helicase. *Science* **2011**, *333*, 1746−1749.

(2) Abbondanzieri, E. A.; Greenleaf, W. J.; Shaevitz, J. W.; Landick, R.; Block, S. M. Direct observation of base-pair stepping by RNA polymerase. *Nature* **2005**, *438*, 460−465.

(3) Greenleaf, W. J.; Woodside, M. T.; Abbondanzieri, E. A.; Block, S. M. Passive all-optical force clamp for high-resolution laser trapping. *Phys. Rev. Lett.* **2005**, *95*, 208102.

(4) Friese, M. E.; Nieminen, T. A.; Heckenberg, N. R.; Rubinsztein-Dunlop, H. Optical alignment and spinning of laser-trapped microscopic particles. *Nature* **1998**, *394*, 348−350.

(5) Vaippully, R.; Bhatt, D.; Ranjan, A. D.; Roy, B. Study of adhesivity of surfaces using rotational optical tweezers. *Phys. Scr.* **2019**, *94*, 105008.

(6) Vaippully, R.; Lokesh, M.; Roy, B. Continuous rotational motion in birefringent particles using two near-orthogonally polarized optical tweezers beams at different wavelengths with low ellipticity. *J. Opt.* **2021**, *23*, 094001.

(7) Ramaiya, A.; Roy, B.; Bugiel, M.; Schäffer, E. Kinesin rotates unidirectionally and generates torque while walking on microtubules. *Proc. Natl. Acad. Sci. U.S.A* **2017**, *114*, 10894−10899.

(8) Koster, D. A.; Croquette, V.; Dekker, C.; Shuman, S.; Dekker, N. H. Friction and torque govern the relaxation of DNA supercoils by eukaryotic topoisomerase IB. *Nature* **2005**, *434*, 671−674.

(9) Strick, T. R.; Croquette, V.; Bensimon, D. Single-molecule analysis of DNA uncoiling by a type II topoisomerase. *Nature* **2000**, *404*, 901−904.

(10) Nguyen, J.; Conca, D. V.; Stein, J.; Bovo, L.; Howard, C. A.; Llorente Garcia, I. Magnetic control of graphitic microparticles in aqueous solutions. *Proc. Natl. Acad. Sci. U. S. A.* **2019**, *116*, 2425−2434.

(11) Conroy, R. *Handbook of molecular force spectroscopy*; Springer: New York, 2008; pp 23−96.

(12) Strick, T. R.; Allemand, J.-F.; Bensimon, D.; Bensimon, A.; Croquette, V. The elasticity of a single supercoiled DNA molecule. *Science* **1996**, *271*, 1835−1837.

(13) Gosse, C.; Croquette, V. Magnetic tweezers: micromanipulation and force measurement at the molecular level. *Biophys. J.* **2002**, *82*, 3314−3329.

(14) Bausch, A. R.; Möller, W.; Sackmann, E. Measurement of local viscoelasticity and forces in living cells by magnetic tweezers. *Biophys. J.* **1999**, *76*, 573−579.

(15) Neuman, K. C.; Nagy, A. Single-molecule force spectroscopy: optical tweezers, magnetic tweezers and atomic force microscopy. *Nat. methods* **2008**, *5*, 491−505.

(16) van Loenhout, M. T.; Kerssemakers, J. W.; De Vlaminck, I.; Dekker, C. Non-bias-limited tracking of spherical particles, enabling nanometer resolution at low magnification. *Biophys. J.* **2012**, *102*, 2362−2371.

(17) Cnossen, J. P.; Dulin, D.; Dekker, N. An optimized software framework for real-time, high-throughput tracking of spherical beads. *Rev. Sci. Instrum.* **2014**, *85*, 103712.

(18) Gosse, C.; Croquette, V. Magnetic tweezers: micromanipulation and force measurement at the molecular level. *Biophys. J.* **2002**, *82*, 3314−3329.

(19) Lansdorp, B. M.; Tabrizi, S. J.; Dittmore, A.; Saleh, O. A. A high-speed magnetic tweezer beyond 10,000 frames per second. *Rev. Sci. Instrum.* **2013**, *84*, 044301.

(20) Huhle, A.; Klaue, D.; Brutzer, H.; Daldrop, P.; Joo, S.; Otto, O.; Keyser, U. F.; Seidel, R. Camera-based three-dimensional real-time particle tracking at kHz rates and Ångström accuracy. *Nat. Commun.* **2015**, *6*, 5885.

(21) Jones, P. H.; Maragó, O. M.; Volpe, G. *Optical Tweezers: Principles and Applications*; Cambridge University Press, 2015.

(22) Neuman, K. C.; Block, S. M. Optical trapping. *Rev. Sci. Instrum.* **2004**, *75*, 2787−2809.

(23) Sarkar, R.; Rybenkov, V. V. A guide to magnetic tweezers and their applications. *Front. Phys.* **2016**, *4*, 48.

(24) De Vlaminck, I.; Dekker, C. Recent advances in magnetic tweezers. *Annu. Rev. Biophys.* **2012**, *41*, 453−472.

(25) Neuman, K. C.; Lionnet, T.; Allemand, J.-F. Single-molecule micromanipulation techniques. *Annu. Rev. Mater. Res.* **2007**, *37*, 33−67.
(26) Zhou, Z.; Miller, H.; Wollman, A. J.; Leake, M. C. Developing a New Biophysical Tool to Combine Magneto-Optical Tweezers with Super-Resolution Fluorescence Microscopy. *Photonics* **2015**, *2*, 758−772.
(27) Crut, A.; Koster, D. A.; Seidel, R.; Wiggins, C. H.; Dekker, N. H. Fast dynamics of supercoiled DNA revealed by single-molecule experiments. *Proc.Natl. Acad. Sci. U.S.A* **2007**, *104*, 11957−11962.
(28) Kumar, S.; Kumar, A.; Gunaseelan, M.; Vaippully, R.; Chakraborty, D.; Senthilselvan, J.; Roy, B. Trapped in out-of-equilibrium stationary state: Hot Brownian motion in optically trapped upconverting nanoparticles. *Front. Phys.* **2020**, *8*, 429.
(29) Kumar, S.; Gunaseelan, M.; Vaippully, R.; Kumar, A.; Ajith, M.; Vaidya, G.; Dutta, S.; Roy, B. Pitch-rotational manipulation of single cells and particles using single-beam thermo-optical tweezers. *Biomed. Opt. Express.* **2020**, *11*, 3555−3566.
(30) Kumar, S.; M, G.; Vaippully, R.; Banerjee, A.; Roy, B. Breaking the diffraction limit in absorption spectroscopy using upconverting nanoparticles. *Nanoscale* **2021**, *13*, 11856−11866.
(31) Tang, J.; Chen, L.; Li, J.; Wang, Z.; Zhang, J.; Zhang, L.; Luo, Y.; Wang, X. Selectively enhanced red upconversion luminescence and phase/size manipulation via Fe 3+ doping in NaYF 4: Yb, Er nanocrystals. *Nanoscale* **2015**, *7*, 14752−14759.
(32) Zhang, Y.; Shen, Y.; Liu, M.; Han, Y.; Mo, X.; Jiang, R.; Lei, Z.; Liu, Z.; Shi, F.; Qin, W. Enhanced high-order ultraviolet upconversion luminescence in sub-20 nm β-NaYbF 4:0.5% Tm nanoparticles via Fe 3. doping. *CrystEngComm* **2017**, *19*, 1304−1310.
(33) Luo, Y.; Chen, Z.; Wen, S.; Han, Q.; Fu, L.; Yan, L.; Jin, D.; Bünzli, J.-C. G.; Bao, G. Magnetic regulation of the luminescence of hybrid lanthanide-doped nanoparticles. *Coord. Chem. Rev.* **2022**, *469*, 214653.
(34) Lokesh, M.; Vaippully, R.; Bhallamudi, V. P.; Prabhakar, A.; Roy, B. Realization of pitch-rotational torque wrench in two-beam optical tweezers. *J. Phys. Commun.* **2021**, *5*, 115016.
(35) Lokesh, M.; Vaippully, R.; Nalupurackal, G.; Roy, S.; Bhallamudi, V. P.; Prabhakar, A.; Roy, B. Estimation of rolling work of adhesion at the nanoscale with soft probing using optical tweezers. *RSC Adv.* **2021**, *11*, 34636−34642.
(36) Vaippully, R.; Ramanujan, V.; Gopalakrishnan, M.; Bajpai, S.; Roy, B. Detection of sub-degree angular fluctuations of the local cell membrane slope using optical tweezers. *Soft Matter* **2020**, *16*, 7606−7612.
(37) Stilgoe, A. B.; Nieminen, T. A.; Rubinsztein-Dunlop, H. Controlled transfer of transverse orbital angular momentum to optically trapped birefringent microparticles. *Nat. Photonics* **2022**, *16*, 346−351.
(38) Lokesh, M.; Nalupurackal, G.; Roy, S.; Chakraborty, S.; Goswami, J.; M, G.; Roy, B. Generation of partial roll rotation in a hexagonal NaYF 4 particle by switching between different optical trapping configurations. *Opt. Express* **2022**, *30*, 28325−28334.
(39) Bonilla-Brunner, A.; Llorente García, I.; Jang, B.; Amano Patino, M.; Alimchandani, V.; Nelson, B. J.; Pane, S.; Contera, S. Polymeric microellipsoids with programmed magnetic anisotropy for controlled rotation using low ($\approx$ 10 mT) magnetic fields. *Appl. Mater. Today* **2020**, *18*, 100511.
(40) Sinha, B.; Anandakumar, S.; Oh, S.; Kim, C. Micro-magnetometry for susceptibility measurement of superparamagnetic single bead. *Sens. Actuator A Phys.* **2012**, *182*, 34−40.
(41) Wu, X.; Tang, Z.; Hu, S.; Yan, H.; Xi, Z.; Liu, Y. NaLuF4: Yb3+, Er3+ bifunctional microcrystals codoped with Gd3+ or Dy3+ ions: enhanced upconversion luminescence and ferromagnetic-paramagnetic transition. *J. Alloys Compd.* **2016**, *684*, 105−111.
(42) Wen, C.; Yin, F.; Cheng, Y.; Yu, H.; Sun, Y.-Q.; Yin, X.-B. Construction of NaYF4 Library for Morphology-Controlled Multi-modality Applications. *Small* **2021**, *17*, 2103206.
(43) Bødker, F.; Hansen, M. F.; Koch, C. B.; Lefmann, K.; Mørup, S. Magnetic properties of hematite nanoparticles. *Phys. Rev. B* **2000**, *61*, 6826.
(44) Tadic, M.; Panjan, M.; Damnjanovic, V.; Milosevic, I. Magnetic properties of hematite (α-Fe2O3) nanoparticles prepared by hydrothermal synthesis method. *Appl. Surf. Sci.* **2014**, *320*, 183−187.
(45) Berg-Sørensen, K.; Flyvbjerg, H. Power spectrum analysis for optical tweezers. *Rev. Sci. Instrum.* **2004**, *75*, 594−612.
(46) Tolić-Nørrelykke, S. F.; Schäffer, E.; Howard, J.; Pavone, F. S.; Jülicher, F.; Flyvbjerg, H. Calibration of optical tweezers with positional detection in the back focal plane. *Rev. sci. instrum* **2006**, *77*, 103101.
(47) Gittes, F.; Schmidt, C. F. Interference model for back-focal-plane displacement detection in optical tweezers. *Opt. lett.* **1998**, *23*, 7−9.
(48) Allersma, M. W.; Gittes, F.; deCastro, M. J.; Stewart, R. J.; Schmidt, C. F. Two-dimensional tracking of ncd motility by back focal plane interferometry. *Biophys. J.* **1998**, *74*, 1074−1085.
(49) Kumar, A.; Gunaseelan, M.; Vaidya, G.; Vaippully, R.; Roy, B. Estimation of motional parameters using emission from upconverting particles optically trapped at the pump wavelength. *Eur. Phys. J.: Spec. Top.* **2022**, *231*, 605.
(50) Rodríguez-Sevilla, P.; Zhang, Y.; de Sousa, N.; Marqués, M. I.; Sanz-Rodríguez, F.; Jaque, D.; Liu, X.; Haro-González, P. Optical torques on upconverting particles for intracellular microrheometry. *Nano Lett.* **2016**, *16*, 8005−8014.
(51) Haro-Gonzalez, P.; del Rosal, B.; Maestro, L. M.; Martín Rodriguez, E.; Naccache, R.; Capobianco, J.; Dholakia, K.; Sole, J. G.; Jaque, D. Optical trapping of NaYF 4: Er 3+, Yb 3+ upconverting fluorescent nanoparticles. *Nanoscale* **2013**, *5*, 12192−12199.
(52) Alapan, Y.; Bozuyuk, U.; Erkoc, P.; Karacakol, A. C.; Sitti, M. Multifunctional surface microrollers for targeted cargo delivery in physiological blood flow. *Sci. Robot.* **2020**, *5*, eaba5726.
(53) Bozuyuk, U.; Alapan, Y.; Aghakhani, A.; Yunusa, M.; Sitti, M. Shape anisotropy-governed locomotion of surface microrollers on vessel-like microtopographies against physiological flows. *Proc. Natl. Acad. Sci. U. S. A.* **2021**, *118*, e2022090118.
(54) Kresse, G.; Joubert, D. From ultrasoft pseudopotentials to the projector augmented-wave method. *Phys. Rev. B* **1999**, *59*, 1758−1775.
(55) Kresse, G.; Furthmüller, J. Efficient iterative schemes for ab initio total-energy calculations using a plane-wave basis set. *Phys. Rev. B* **1996**, *54*, 11169−11186.

https://doi.org/10.1021/acsaom.2c00161
ACS Appl. Opt. Mater. 2023, 1, 615−622

Supporting Information: Simultaneous optical trapping and electromagnetic micromanipulation of ferromagnetic doped-$NaYF_4$ microparticles

Gokul Nalupurackal[1], Gunaseelan M.[1,2], Muruga Lokesh[1], Rahul Vaippully[1], Amit Chauhan[3], B. R. K. Nanda[3], Chandran Sudakar[4], Hema Chandra Kotamarthi[5], Priyankan Datta[6], Pallab Sinha Mahapatra[6], Anita Jannasch[7], Erik Schäffer[7], Jayaraman Senthilselvan[8], and Basudev Roy[1,*]

[1]*Department of Physics, Quantum Centres in Diamond and Emergent Materials (QuCenDiEM)-group, Micro Nano and Bio-Fluidics (MNBF)-Group, Indian Institute of Technology Madras, Chennai, India 600036*

[2]*Department of Physics, Rathinam Research Hub, Rathinam College of Arts and Science, Coimbatore, India 641021*

[3]*Condensed Matter Theory and Computational Lab, Department of Physics, Indian Institute of Technology Madras, Chennai - 600036, India*

[4]*Center for Atomistic Modelling and Materials Design, Indian Institute of Technology Madras, Chennai - 600036, India*

[5]*Department of Chemistry, Indian Institute of Technology Madras, Chennai, India, 600036*

[6]*Department of Mechanical Engineering, Indian Institute of technology Madras, Chennai, India, 600036*

[7]*Center for Plant Molecular Biology (ZMBP), University of Tübingen, Germany*

[8]*Department of Nuclear Physics, University of Madras, Chennai, India, 600025*

[*]*basudev@iitm.ac.in*

Contents

1 Optical tweezers set-up. **S3**

2 T-matrix calculation of trapping feasibility of Fe-NYF **S4**

3 Morphological properties and elemental composition of Fe-doped UCPs. **S5**

3.1 The material. S6

3.2 X-ray diffraction spectra of Fe-15 NYF. S6

3.3 X-ray photoelectron spectra of Fe-15 NYF. S8

4 Absorption and emission properties. **S10**

4.1 Refractive index measurements using spectroscopic ellipsometry S11

5 Magneto-optical tweezers. **S12**

1 Optical tweezers set-up.

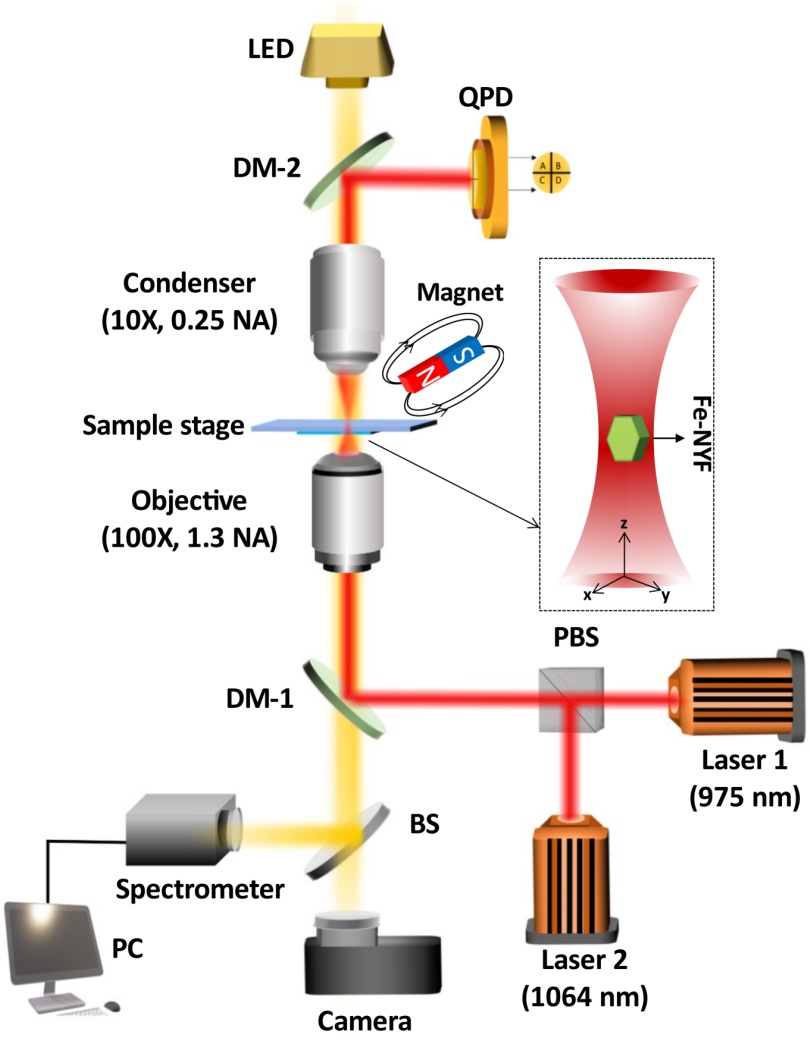

Figure S1: This figure represents the schematic diagram of the experiment. The entire setup consists of a single beam optical tweezers configured as an inverted microscope and its detection units. The optical trap is created near the focus of the 100x, 1.3 N.A objective and the entire sample chamber is illuminated by an LED through a dichroic mirror as shown in the figure. DM - Dichroic mirror, PBS - Polarising beam splitter, BS - 50:50 beam splitter, QPD - Quadrant photo diode.

2 T-matrix calculation of trapping feasibility of Fe-NYF

Optically trapping iron-oxide particles is known to be difficult, particularly if they are larger than a certain size [1]. We investigate why that is the case and examine our Fe NYF particles towards suitability of trapping. The optical tweezers operation can be fundamentally treated as a scattering problem [2]. The particles of choice are frequently homogeneous and isotropic with spherical symmetry, for which an analytical solution to the scattering problem uses the generalized Lorentz-Mie theory (GLMT) [3] or the transfer matrix approach.

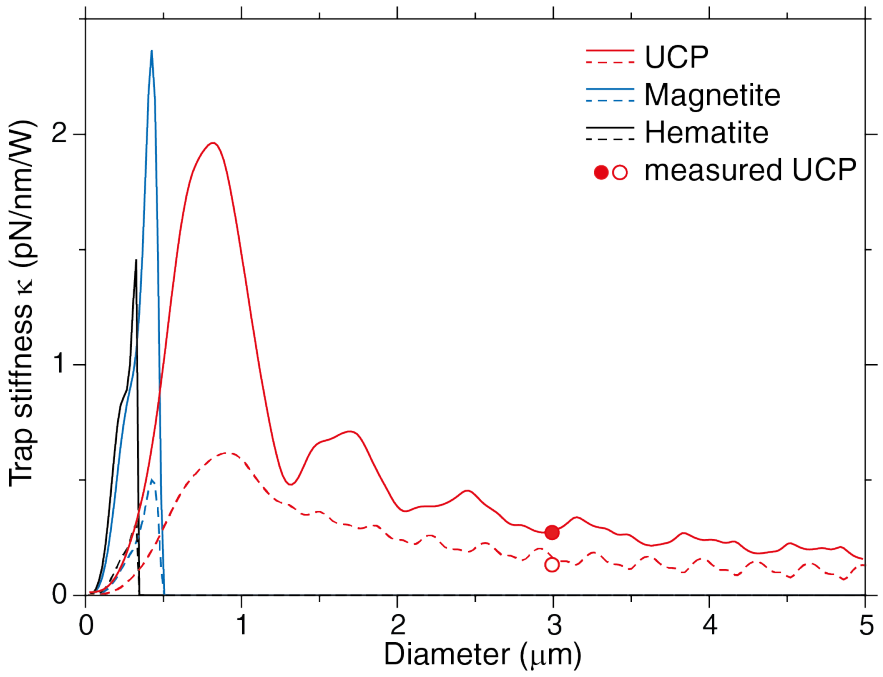

Figure S2: Lateral (solid lines) and axial (dashed lines) trap stiffness of magnetite, hematite and UCP particles as function of their diameter. The red solid (circle) data point represent the measured lateral (axial) trap stiffness of 3 µm UCP hexagonal particles. The scattering calculations are based on Mie-Theory. Here, the imaginary components of refractive index, implying absorption, has not been considered for Haematite and Magnetite. The trappable size reduces even further if the absorption is considered.

We use this T-matrix method to perform optical trapping stability calculations using the optical tweezers toolbox [2, 4]. We specify the parameters for the computation: refractive indices, $n_{Fe-15NYF} = 1.476 + i\ 0.0011$, $n_{NYF} = 1.461 + i\ 0.0008$, $n_{hematite} = 2.504 + i\ 0.038$, $n_{magnetite} = 2.112 + i\ 0.365$, at a laser wavelength of 1064 nm, Numerical Aperture (NA) =1.3 and linearly polarized light. The parameters for the Fe-NYF and NYF have been measured from ellipsometry. We calculate the lateral and axial trap stiffness as function of the diameter (Fig. S2), assuming spherical particles. We find that due to their high refractive indices, magnetic Fe-oxide particles, like magnetite and hematite, are only stably trappable till a small diameter (up to 400 nm). It may be noted here that the imaginary components of the refractive index (absorption) of haematite and magnetite have been ig-

nored for this calculation. If these are included, the stable trapping diameter reduces even further. In contrast, Fe-doped upconversion particles have a low refractive index comparable to silica which allows them to be stably trapped in all three dimensions even for diameters of several micrometers. For example, 3 µm diameter spherical NYF's have a theoretical lateral (axial) trap stiffness of 0.36 pN/nm/W (0.15 pN/nm/W) that is in good agreement with the experimentally measured lateral (axial) trap stiffness of 0.26 ± 0.03 pN/nm/W (0.12±0.011 pN/nm/W; mean±SD, N=10). It can be noted here that the optical trapping of such Fe-15 NYF is minimally affected by the absorption due to the Fe atoms where the imaginary part of the refractive index increases only marginally.

3 Morphological properties and elemental composition of Fe-doped UCPs.

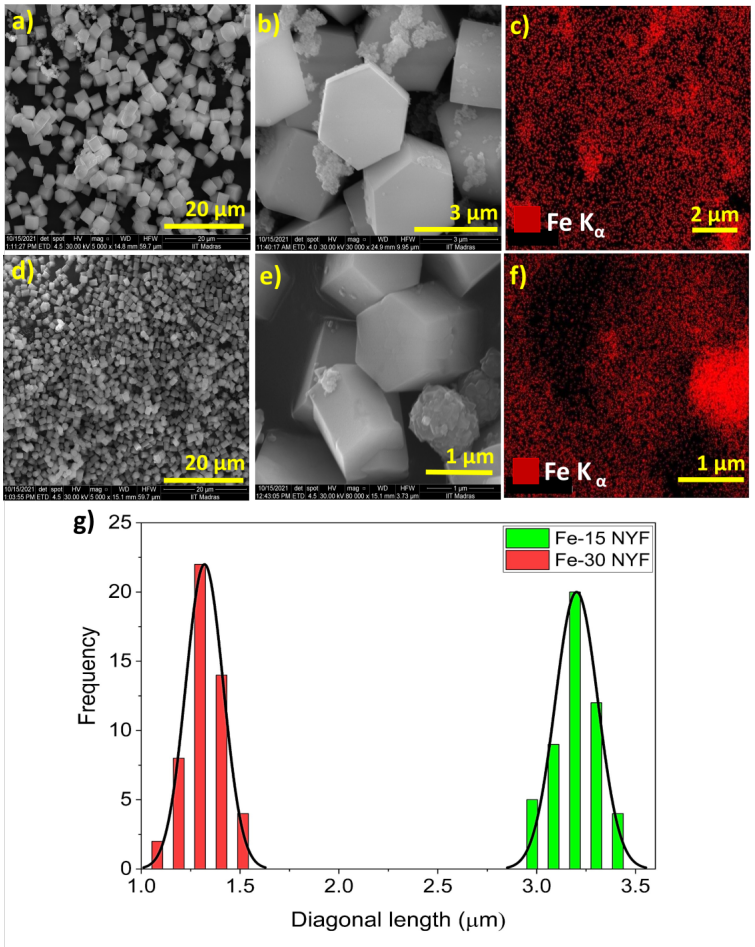

Figure S3: The FE-SEM images of Fe-15 and Fe-30 NYF upconversion particles are shown in figures(a-b) and (d-e) respectively. Figures(c) and (f) represents the elemental mapping of iron corresponding to figures (b) and (e) respectively. (g) shows the diagonal length distributions of Fe-30 NYF and Fe-15 NYF obtained from FESEM data.

3.1 The material.

The Fe doped $NaYF_4$:Yb,Er upconversion particles (Fe-NYF) with sizes larger than 2 μm were prepared using hydrothermal process. The field emission scanning electron microscope (FE-SEM) images and the corresponding energy dispersive x-ray spectroscopy (EDS) elemental maps for the particles with different degrees of doping (15 at.% and 30 at.%, Fe-15NYF and Fe-30 NYF, respectively) are shown in Fig.S3(a-f) of supplimentary information. The Fe-NYF are formed as precise hexagonal shaped particles with different sizes. The estimated average side length $\times$ width are 3.2 μm $\times$ 2.8 μm and 1.3 μm $\times$ 1.4 μm for Fe-15 and Fe-30 NYFs, respectively. The EDS element mappings were performed to confirm the presence of Fe in the crystal lattice. The Fe K_α elemental maps from the regions shown in Fig.S3(b and e). These elemental maps reveal the existence of uniformly distributed Fe in the hexagonal Fe-NYF. In addition, few Fe-rich particles with no definite morphological feature, mostly from α-Fe_2O_3 impurities, are seen lying next to these Fe-NYF.

3.2 X-ray diffraction spectra of Fe-15 NYF.

Fig.S4 shows the X-ray diffraction (XRD) pattern (red dots) for the NYF, Fe-15 NYF and Fe-30 NYF. The Rietveld refinement performed using the FullProf software with the simulated pattern and obtained with a best χ^2 is shown in black line [5, 6]. The prepared samples crystallize in hexagonal structure of $NaYF_4$ (β-$NaYF_4$) with the space group of $P6_3/m$. Despite the substitution of Fe^{3+} at the Y^{3+} site the structure remains in the hexagonal phase. The estimated lattice parameters are shown in table S4(d) and match well with the structure of β-$NaYF_4$ (JCPDS No.: 16-0334). In addition to the β-$NaYF_4$, the samples exhibit small phase fraction of α-Fe_2O_3 impurity (0.96 wt.%). If Fe does not go into the lattice of β-$NaYF_4$ structure, the diffraction pattern would show 13 wt.% α-Fe_2O_3 impurity phase. Fe-30NYF samples also show β-$NaYF_4$ structure as shown in Fig. S4(c), however, with higher percentage of α-Fe_2O_3 (2.5 wt.%) phase. For the present study we have used Fe-15NYF's as it exhibits optimal magnetization values need for the optical trapping experiments.

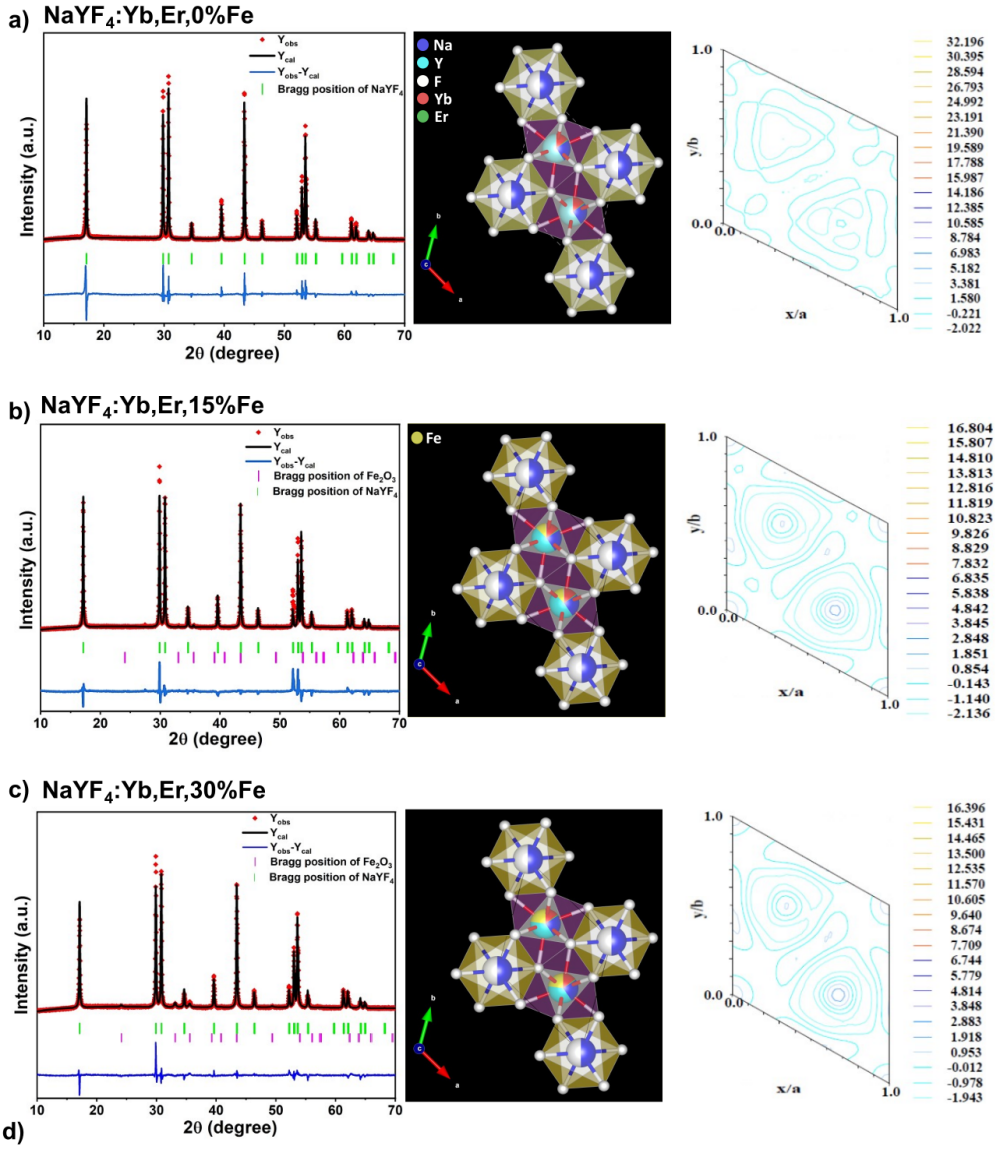

d)

Materials	Lattice Parameters (Å)	Ln-Ln bond length (Å)	Unit cell volume (Å^3)	R-factor (%)	Phase fraction of hexagonal $NaYF_4$ (%)
$NaYF_4$:Yb,Er (NYF)	a=b=5.9902(6); c= 3.5114(6)	3.8786(2)	109.122	7.74	100
Fe-15 NYF	a=b=5.9815(1); c= 3.5055(7)	3.8727(8)	108.620	6.28	99.04
Fe-30 NYF	a=b=5.9798(7); c= 3.5031(5)	3.8713(9)	108.486	4.30	94.96

Figure S4: The figure shows the X-ray diffraction(XRD) spectra with Rietveld refinement, simulated crystal field structure and the corresponding Fourier maps of (a) Bare NYF (b) Fe-15 NYF (c) Fe-30 NYF respectively. Black lines are corresponding to the simulated XRD spectra using Rietveld refinement method of best χ^2 and R-factor. In table(d), the crystallographic parameters obtained from simulated crystal structures of the particles are shown.

3.3 X-ray photoelectron spectra of Fe-15 NYF.

The X-ray photoelectron spectroscopy (XPS) was used to confirm the valency of elements in the Fe-NYF's and estimate the at.% of elements in the compound. A representative analyses of XPS spectra performed on $NaYF_4$:Yb,Er NYF's and Fe-15 NYF is shown in the Fig.S5 of supplementary material. The survey spectrum shown in Fig.S5(a) clearly shows the presence of Na, Y, F, Yb and Er elements in the sample. In addition, XPS signals from dopant Fe are clearly discerned. The strong signals from Na 1s, Y 3d and F 1s spectra shown in Fig.S5(b-d) confirm the formation of $NaYF_4$. Further, the presence of Yb and Er 4d spectra lines are detectable despite the signal arising from few tens of Angstrom layers of the surface region as shown in Fig.S5(e). The binding energy of photoelectrons from all these elements, viz Na (+1), Y (+3), F (-1), Yb (+3) and Er (+3), suggests that the oxidation states are consistent with the known composition. Further the integral intensity used to estimate the composition also confirm the nominal composition taken in the synthesis. The 2p photoelectron spectra from the element Fe is indicating the +3 oxidation state with Fe $2p_{3/2}$ peaks appearing at 711 eV. Due to the oxidation state and favorable ionic size we expect that the Fe atoms mostly occupy Y sites which is also occupied by the Yb and Er dopants. The estimates on the Fe concentration is also consistent with the nominal concentration taken during the synthesis. The high resolution spectral features of the elements in the pristine $NaYF_4$:Yb,Er(NYF) and Fe doped $NaYF_4$:Yb,Er (Fe-NYF) are similar, specifically shown in Fig.S5(g) for Yb and Er XPS spectra. This strongly suggests that Fe-15 NYF particles are compositionally similar to the pristine compounds of $NaYF_4$:Yb,Er and that preferably Fe ions occupy Y^{3+} sites as it has 3+ valence state.

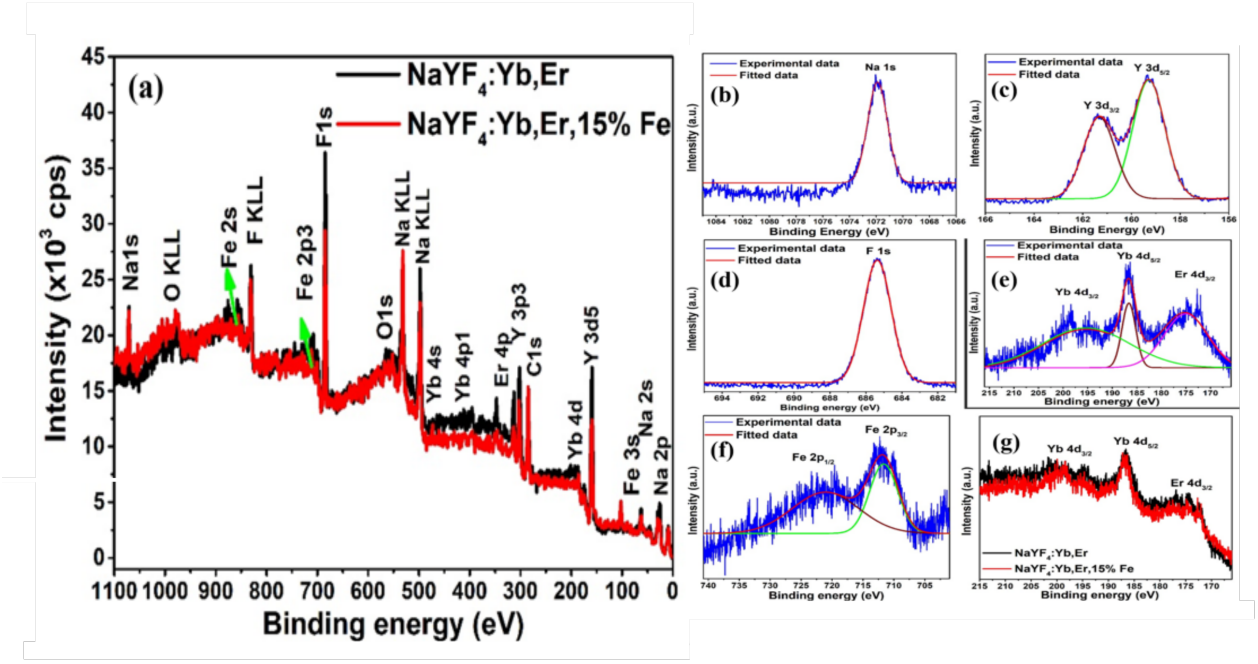

Figure S5: The X-ray photoelectron spectra of Fe-15 NYF is shown in the above figure. In (a) Survey spectra, (b) Na 1s, (c) Y 3d, (d) F 1s, (f) Fe 2p and (e,g) Yb 4d, Er 4d. are shown. This is used to confirm the valency of elements in the Fe-NYF's and estimate the at.% of elements in the compound. The survey spectrum shown in (a) clearly shows the presence of Na, Y, F, Yb and Er elements in the sample. In addition, XPS signals from dopant Fe are clearly discerned. The strong signals from Na 1s, Y 3d and F 1s spectra shown in (b-d) confirm the formation of $NaYF_4$. Further, the presence of Yb and Er 4d spectra lines are detectable despite the signal arising from few tens of Angstrom layers of the surface region as shown in Fig.S3(e). The binding energy of photoelectrons from all these elements, viz Na (+1), Y (+3), F (-1), Yb (+3) and Er (+3), suggests that the oxidation states are consistent with the known composition. Further the integral intensity used to estimate the composition also confirm the nominal composition taken in the synthesis. The 2p photoelectron spectra from the element Fe is indicating the +3 oxidation state with Fe $2p_{3/2}$ peaks appearing at 711 eV. Due to the oxidation state and favorable ionic size we expect that the Fe atoms mostly occupy Y sites which is also occupied by the Yb and Er dopants. The estimates on the Fe concentration is also consistent with the nominal concentration taken during the synthesis. The high resolution spectral features of the elements in the pristine $NaYF_4$:Yb,Er(NYF) and Fe doped $NaYF_4$:Yb,Er (Fe-NYF) are similar, specifically shown in (g) for Yb and Er XPS spectra. This strongly suggests that Fe-15 NYF particles are compositionally similar to the pristine compounds of $NaYF_4$:Yb,Er and that preferably Fe ions occupy Y^{3+} sites as it has 3+ valence state.

4 Absorption and emission properties.

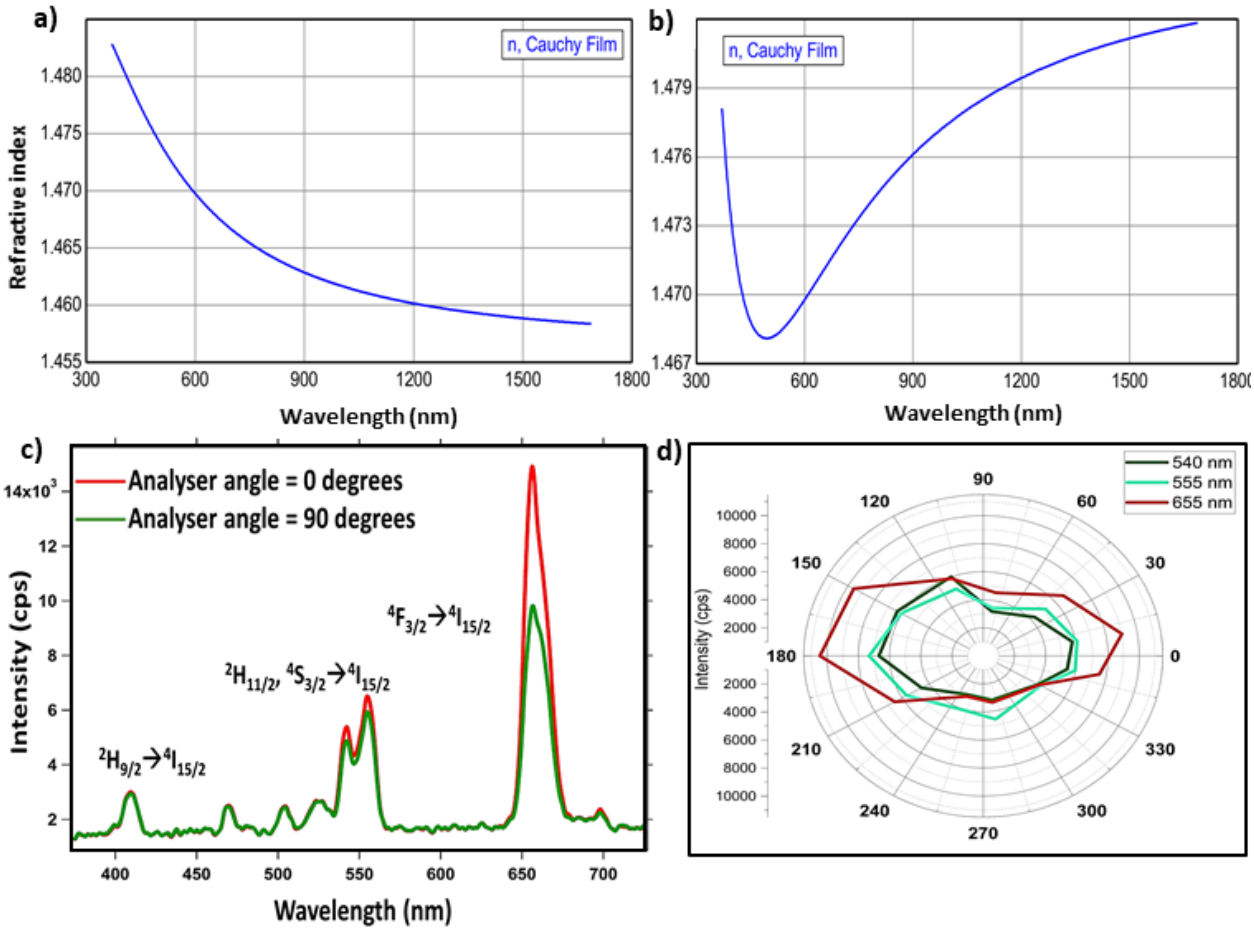

Figure S6: Wavelength dependence of real part of refractive indices of a) NYF UCP and b) Fe-15 NYF are shown in the figure. (c) shows emission spectrum of Fe-15 NYF, recorded at orthogonal angles of a polariser with respect to the side-on axis of the particle under the illumination of 975 nm laser. When a hexagonal UCP is optically trapped, it prefers to orient with the side-on axis facing the tweezers beam. The beam intensity is measured to be 1 MW/cm^2. d) represents the polar plot of emission intensities of a single Fe-15 NYF, plotted as a function of angle between it's side on axis and pass axis of a polariser.

4.1 Refractive index measurements using spectroscopic ellipsometry

The refractive index measurements of Fe-15 NYF particles are carried out using a spectroscopic ellipsometer (Woollam S.E M-2000VI EC-400). It requires a thin film of the sample crystals having uniform thickness. To meet this, 5 mg of Fe-15 NYF and NYF UCP particles are dispersed in 1 mL of DMS (dimethyl sulphate) and the solution is coated on a silicon substrate (25mm×25mm) using a spin coater at 1500 RPM. The light source of variable

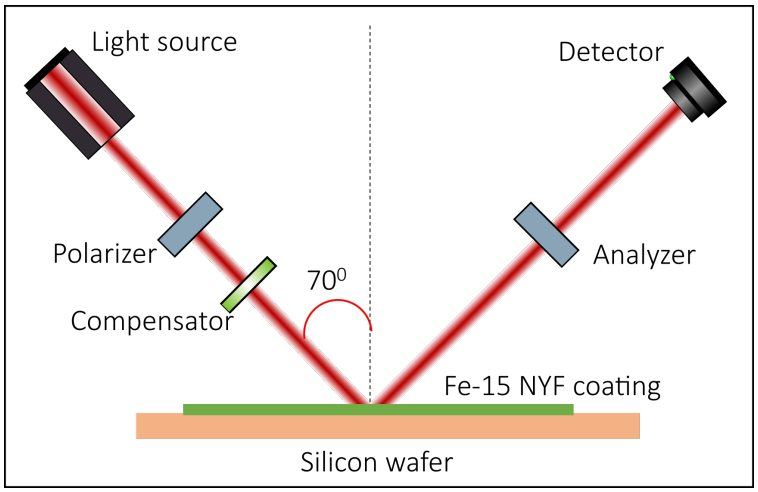

Figure S7: Schematic depiction of spectroscopic ellipsometry.

wavelength (500 - 1200 nm) is made to incident at an angle 70°, at the region were the film thickness is found to be uniform, as shown in Fig.S7. Refractive index of the sample was determined by constructing optical model and optical fitting using [7],

$$\rho = \frac{r_p}{r_s} = tan\psi \times exp(\iota\Delta) \tag{1}$$

With ρ is the reflectivity, r_p/r_s is the reflectivity ratio of p- and s-polarized light waves, ψ is the amplitude ratio and Δ is the phase difference between them. The refractive index can be written as $N = n - i\ k$, where n is the real part and k is the extinction coefficient. This can be obtained by fitting the following equations,

$$r_p = \frac{n_t cos\theta_i - n_i cos\theta_t}{n_t cos\theta_i + n_i cos\theta_t} \tag{2}$$

$$r_s = \frac{n_i cos\theta_i - n_t cos\theta_t}{n_i cos\theta_i + n_t cos\theta_t} \tag{3}$$

And from the absorption coefficient α,

$$k = \frac{\alpha\lambda}{4\pi} \tag{4}$$

Where, indices of i and t represent incident and transmission conditions. The obtained values of real part of refractive indices are plotted as a function of wavelength (see S6(a-b)) and the values of extinction coefficients for Fe-30 NYF and NYF UCP at 980 nm and 1050 nm are tabulated in table 1.

Table 1: The refractive index values.

Wavelength (nm)	Particle	n	k
980	NYF UCP (0% Fe)	1.463	0.0014
	Fe-15 NYF	1.479	0.0029
1050	NYF UCP (0% Fe)	1.461	0.0008
	Fe-15 NYF	1.477	0.0011

5 Magneto-optical tweezers.

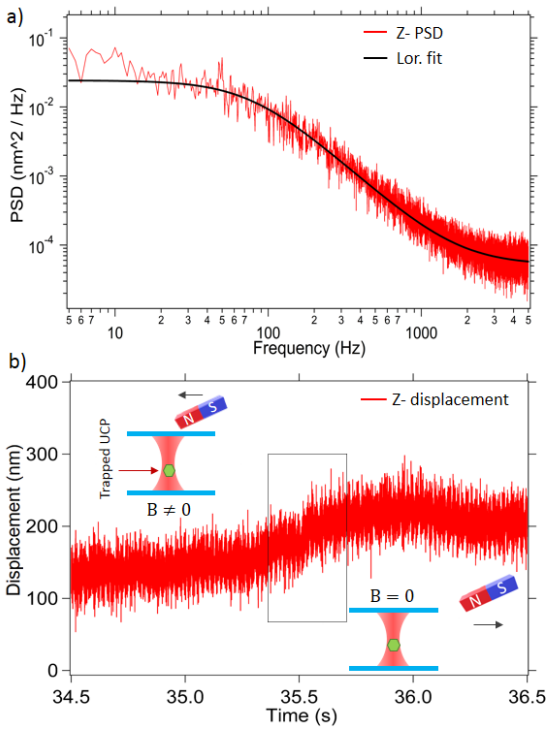

Figure S8: The power spectral density of perpendicular displacements (z-displacements) of an optically trapped Fe-15 NYF is shown in Fig (a). The optical trap is calibrated with a displacement sensitivity of 1.0 ± 0.1 μm / volt. The corner frequency (fc) is 103 ± 10 Hz. In (b), the calibrated perpendicular displacement(z) time series of a Fe-15 NYF in the optical trap, exposed to an external magnetic field (B) generated by an electromagnet is shown. The marked region in the time series indicates the time interval during which the field, B is turned off.

References

[1] A. Samadi, M. Wang, Y. Yang, and L. B. Oddershede, "Optical trapping of individual magnetic nanoparticles," in *Optical Trapping and Optical Micromanipulation XV*, vol. 10723. International Society for Optics and Photonics, 2018, p. 107230.

[2] T. A. Nieminen, V. L. Loke, A. B. Stilgoe, G. Knöner, A. M. Brańczyk, N. R. Heckenberg, and H. Rubinsztein-Dunlop, "Optical tweezers computational toolbox," *J. Opt. A- Pure. Appl. Op.*, vol. 9, no. 8, p. S196, 2007.

[3] G. Gouesbet, G. Grehan, and B. Maheu, "Localized interpretation to compute all the coefficients gnm in the generalized lorenz–mie theory," *JOSA A*, vol. 7, no. 6, pp. 998–1007, 1990.

[4] T. A. Nieminen, V. L. Loke, A. B. Stilgoe, N. R. Heckenberg, and H. Rubinsztein-Dunlop, "T-matrix method for modelling optical tweezers," *J. Mod. Opt.*, vol. 58, no. 5-6, pp. 528–544, 2011.

[5] J. Rodríguez-Carvajal, "Fullprof," *CEA/Saclay, France*, 2001.

[6] R. Young, *The Rietveld method*, 1993, vol. 5.

[7] H. Fujiwara, *Spectroscopic ellipsometry: principles and applications*. John Wiley & Sons, 2007.